Oral presentation | Reduced order models
Reduced order models-I
Mon. Jul 15, 2024 10:45 AM - 12:45 PM Room C

[1-C-01] Reduced-order Modeling for Pressure Field via Global Proper Orthogonal Decomposition

*Yuto Nakamura[1], Shintaro Sato[1], Naofumi Ohnishi[1] (1. Tohoku University)

Keywords: Proper Orthogonal Decomposition, Reduced-order Model, Incompressible Flow

Twelfth International Conference on Computational Fluid Dynamics (ICCFD12), Kobe, Japan, July 14-19, 2024

ICCFD12-2024-1-C-01

Reduced-Order Modeling for Pressure Field via Global Proper Orthogonal Decomposition

Y. Nakamura*, S. Sato*, and N. Ohnishi*
Corresponding author: yuto.nakamura.t4@dc.tohoku.ac.jp * Tohoku University, Japan.

Abstract: In this study, data-driven reduced-order models (ROM) for pressure fields are constructed. We focus on the system robustness to accurately predict pressure fields differing in Reynolds number (Re) from those in the dataset. The ROM of the pressure field solves a reduced-order equation obtained by Galerkin projection for the pressure Poisson equation using the proper orthogonal decomposition (POD) mode of the pressure field. The ROM is constructed using the POD modes obtained from the time series pressure field around a circular cylinder at $Re = 80$. The mean squared error with the pressure field obtained from full-order numerical simulations is quite large when predicting the pressure field at different Re from the dataset. Conversely, when the dataset includes the pressure fields of $Re = 80$ and 160, the mean squared error is smaller than the ones from the ROM using the $Re = 80$ POD modes, even for pressure fields different from those in the dataset. The ROM is constructed by changing the number of POD modes. For ROMs constructed on datasets containing pressure fields at $Re = 80$ and 160, we found that increasing the number of modes improves robustness. Adding $Re = 120$ to the dataset resulted in smaller mean squared errors between the pressure fields obtained from full-order numerical simulations and those obtained from the ROM for most Re cases. Based on these investigations, a simple approach to the POD that includes the pressure fields of multiple Re in the dataset improves the robustness of the ROM.

Keywords: Reduced-order model, Proper orthogonal decomposition, Pressure estimation, Galerkin projection.

1 Introduction

A reduced-order model (ROM)[1, 2, 3, 4, 5, 6] is known as a faster method of computing flow fields than conventional computational fluid dynamics (CFD). Most ROMs are constructed in a data-driven and empirically based on the CFD results or experiment data. A typical ROM construction method is a model using proper orthogonal decomposition (POD)[7, 8, 9, 10, 11, 12]. The POD is a method of computing the optimal modes to represent a given time-series dataset of flow fields. The flow field is reconstructed from the optimal modes in the POD-based ROM.

In many practical cases, the CFD and ROM solutions depend on parameters such as Reynolds number (Re). In the ROM construction, the flow field given as a dataset contains flow fields under some representative conditions. Therefore, the flow field prediction requires robustness to predict flow fields that differ from the dataset. POD-based ROMs tend to lack this robustness. Various approaches have been proposed to improve the robustness of POD-based ROMs[13, 14, 15, 16, 17, 18, 19, 20].

A flow field with two or more conditions is required for the dataset to improve the robustness of ROM based on the POD. The most simple approach is to apply POD to a dataset that contains flow fields for two or more conditions referred to as global POD[21, 22, 23, 19, 24]. The global POD has the advantage of requiring no complicated algorithms than the POD for a single condition. In this method, the flow fields for multiple conditions are given as a single dataset, and a set of POD modes represents the global characteristics of the flow field for all conditions. However, the global POD-based ROM loses computational stability when more than three conditions are included in the dataset. Even for a simple flow field, as the number of conditions increases, the basis required for the representing datasets becomes enormous. These aspects are clearly shown in the results of applying the global POD to the velocity field[19].

Most of the ROM studies using the POD are to predict velocity fields because the velocity field and derived kinematic properties have played an important role in investigating unsteady flows and turbulence. However, the fluid flow also has a dynamic aspect represented by hydrodynamic pressure. Fluctuating pressure is a primary factor in turbulence, cavitation, and aeroacoustic phenomena[25]. Therefore, estimating the pressure field is just as important as computing the velocity field.

Only a few studies have been conducted regarding the ROM for the pressure field. Akhtar et al.[26, 27] proposed a model to compute the pressure field from a given velocity field using the POD modes, which is obtained by the time-series pressure field. They focused on constructing the ROM for pressure fields and not predicting pressure fields for conditions different from the POD modes. To our knowledge, the pressure field has never been reconstructed in this pressure ROM under conditions different from those of the POD dataset. This study focuses on the robustness of the ROM for pressure fields.

Section 2 formulates the POD methodology and the ROM based on the pressure Poisson equation. Section 3 describes the numerical simulation methods used to prepare the datasets required for the POD. The dataset contains a flow around a cylinder obtained from two-dimensional numerical simulations. In Section 4, we present the ROM results for the pressure field, focusing on the ROM results of varying the Re of pressure fields in the dataset to obtain the POD mode. We emphasize the results for the case involving datasets containing pressure fields of multiple Re's. Section 5 is a summary of this study.

2 Pressure ROM Methodology

2.1 POD

The POD is a method for computing the orthogonal modes $\boldsymbol{\varphi}_k(\boldsymbol{x})$ that best represent a given dataset $\boldsymbol{q}_m(\boldsymbol{x})$ $(m = 1, 2, 3, \cdots, m_{\max})$. The POD is formulated by finding the orthogonal modes $\boldsymbol{\varphi}_k(\boldsymbol{x})$ that satisfy the following minimization problem

$$\underset{\{\boldsymbol{\varphi}_k\}_{k=1}^{r}}{\operatorname{argmin}} \sum_{m=1}^{m_{\max}} \|\tilde{\boldsymbol{q}}_m(\boldsymbol{x}) - \sum_{k=1}^{r} a_{k,m}\boldsymbol{\varphi}_k(\boldsymbol{x})\|^2, \tag{1}$$

where $\tilde{\boldsymbol{q}}_m(\boldsymbol{x})$ represents the fluctuating component of data $\boldsymbol{q}_m(\boldsymbol{x})$ computed below:

$$\tilde{\boldsymbol{q}}_m(\boldsymbol{x}) = \boldsymbol{q}_m(\boldsymbol{x}) - \bar{\boldsymbol{q}}(\boldsymbol{x}), \tag{2}$$

$$\bar{\boldsymbol{q}}(\boldsymbol{x}) = \frac{1}{m_{\max}} \sum_{m=1}^{m_{\max}} \boldsymbol{q}_m(\boldsymbol{x}), \tag{3}$$

and $a_{k,m}$ is the coefficient of the POD mode satisfying below:

$$a_{k,m} = \langle\, \boldsymbol{q}_m(\boldsymbol{x}), \boldsymbol{\varphi}_k(\boldsymbol{x}) \,\rangle. \tag{4}$$

Here, $\langle\, \cdot, \cdot \,\rangle$ represents inner product defined by:

$$\langle\, \boldsymbol{b}(\boldsymbol{x}), \boldsymbol{c}(\boldsymbol{x}) \,\rangle = \int_V \boldsymbol{b}^T(\boldsymbol{x})\boldsymbol{c}(\boldsymbol{x})\, d\boldsymbol{x}, \tag{5}$$

where $\boldsymbol{b}(\boldsymbol{x})$ and $\boldsymbol{c}(\boldsymbol{x})$ represent vector-valued function depending on $\boldsymbol{x}$, and V is the entire domain in which $\boldsymbol{x}$ is defined. Therefore, the reconstruction error is minimized when the data are expressed by the r POD modes as follows:

$$\boldsymbol{q}_m(\boldsymbol{x}) \approx \bar{\boldsymbol{q}}(\boldsymbol{x}) + \sum_{k=1}^{r} a_{k,m}\boldsymbol{\varphi}_k(\boldsymbol{x}). \tag{6}$$

This paper uses snapshot POD[28] and incremental POD[29, 30] to compute the POD mode numerically. Validation of incremental POD is shown in Appendix A.

2.2 Pressure Model

The ROM of the pressure field is constructed by projecting the pressure Poisson equation onto the low-dimensional space spanned by the POD modes[26]. Using the POD mode $\psi_k(\boldsymbol{x})$ obtained from the pressure field data, the pressure field can be decomposed as follows:

$$p(\boldsymbol{x}) \approx \bar{p}(\boldsymbol{x}) + \sum_{k=1}^{r} b_k\psi_k(\boldsymbol{x}), \tag{7}$$

where $\bar{p}(\boldsymbol{x})$ represents average of the pressure, and b_k is coupling coefficients for the POD modes. Under this decomposition, the pressure Poisson equation is projected below:

$$\frac{1}{\rho}\nabla^2\bar{p} + \frac{1}{\rho}\sum_{k=1}^{r} b_{k,m}\nabla^2\psi_k = -\nabla\cdot(\nabla\cdot\boldsymbol{u}_m\boldsymbol{u}_m), \tag{8}$$

where variables with a subscript m represent variables with the same conditions and at the same time. The inner product with the POD mode yields the simultaneous equations for $b_{k,m}$ presented below:

$$\sum_{k=1}^{r} b_{k,m}I_{k,l} = J_l \ \ (l = 1, 2, \cdots, r), \tag{9}$$

$$\begin{aligned} I_{k,l} &= \frac{1}{\rho}\int_V (\nabla^2\psi_k)\psi_l \, d\boldsymbol{x}, \\ J_l &= \int_V \left\{\frac{1}{\rho}\nabla^2\bar{p} - \nabla\cdot(\nabla\cdot\boldsymbol{u}_m\boldsymbol{u}_m)\right\}\psi_l \, d\boldsymbol{x}. \end{aligned} \tag{10}$$

Once the velocity field is given by the velocity ROM, $b_{k,m}$ can be obtained using these equations, and the pressure field can be calculated by Eq. (7). In this study, the velocity field is given by full-order numerical simulation to evaluate the performance of pressure ROM without the error derived from velocity ROM.

3 Data Preparation

3.1 Numerical Simulation Method

This paper uses the flow fields around a circular cylinder for the POD dataset. The dataset is prepared using the numerical simulation of the incompressible Navier-Stokes equations presented below:

$$\nabla\cdot\boldsymbol{u} = 0, \tag{11}$$

$$\frac{\partial\boldsymbol{u}}{\partial t} = -\nabla\cdot\boldsymbol{u}\boldsymbol{u} - \frac{1}{\rho}\nabla p + \frac{1}{Re}\nabla^2\boldsymbol{u}, \tag{12}$$

where Re represents Reynolds number defined using the mainstream velocity U_∞, the kinematic viscosity ν, and characteristic length D as follows:

$$Re = \frac{U_\infty D}{\nu}. \tag{13}$$

The cylinder diameter is used for characteristic length. The governing equations are transformed into a curvilinear coordinate system (ξ^1, ξ^2)

$$\sum_{j=1}^{2}\frac{1}{J}\frac{\partial}{\partial\xi^j}\left(JU^j\right) = 0, \tag{14}$$

$$\begin{aligned} \frac{\partial u_i}{\partial t} = &-\sum_{j=1}^{2}\frac{1}{J}\frac{\partial}{\partial\xi^j}\left(JU^j u_i\right) \\ &+\sum_{j=1}^{2}\frac{1}{\rho}\frac{\partial\xi^j}{\partial x_i}\frac{\partial p}{\partial\xi^j} + \sum_{j=1}^{2}\frac{1}{Re}\frac{1}{J}\frac{\partial}{\partial\xi^j}\sum_{k=1}^{2}\left(\gamma^{jk}\frac{\partial u_i}{\partial\xi^k}\right) \ \ (i = 1, 2), \end{aligned} \tag{15}$$

where

$$\gamma^{jk} = \sum_{l=1}^{2} J\frac{\partial\xi^j}{\partial x_l}\frac{\partial\xi^k}{\partial x_l}, \tag{16}$$

represents a symmetric tensor, u_i is the ith component of Cartesian velocity vector, U^j is the jth component of contravariant component vector, and J is a Jacobian.

The fractional step method[31] is used for temporal discretization of governing equations. The third-

order three-stage Runge–Kutta scheme and the second-order implicit Crank–Nicholson scheme are used for the time integration. The predicted velocity in the fractional step method is corrected to satisfy the continuity equation only in the final stage of the Runge-Kutta method. The spatial discretization is evaluated by the second-order central difference[32] and QUICK method[33]. The pressure Poisson equation is solved using the BiCGstab[34] method with incomplete LU decomposition[35, 36].

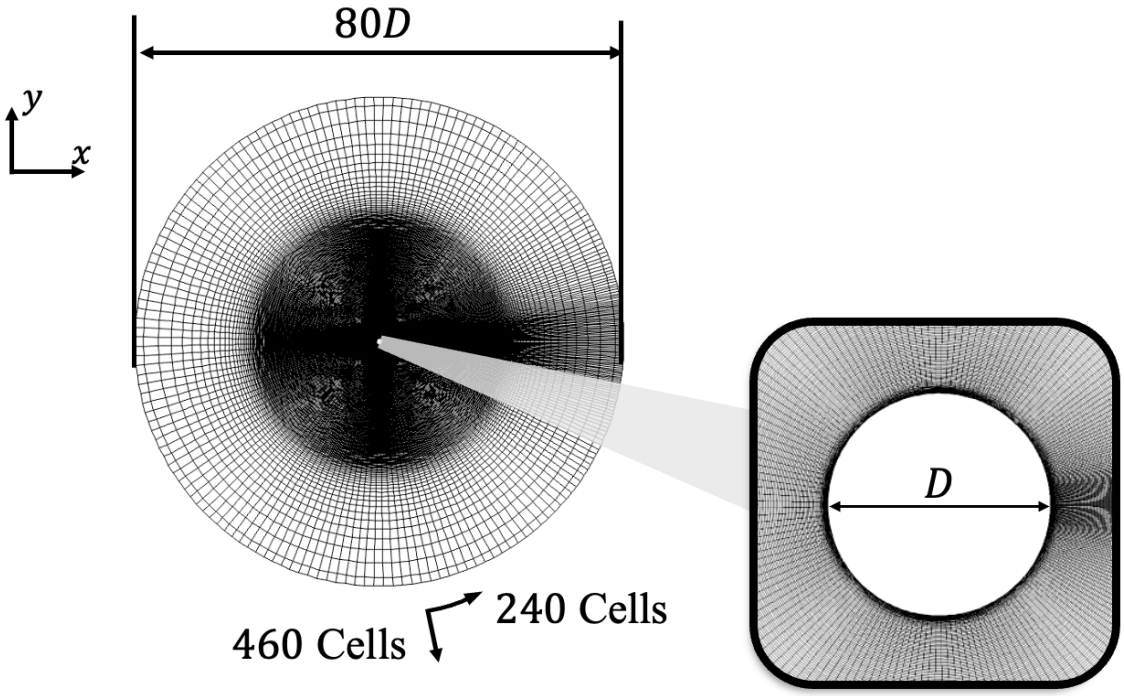

Figure 1: Computational grid around a circular cylinder. The characteristic length in Re is the cylinder diameter D. The inflow and outflow boundary are set at 80 times the cylinder diameter.

3.2 Grid and Time Dependancy

We evaluate the computational grid and time step size dependency in numerical simulations with regular and fine grids. The regular computational grid around a cylinder is shown in Fig. 1. The far-field boundary of the computational grid extends up to 80 times the diameter of a circular cylinder D. The number of cells is 240 in the wall-normal direction and 460 in the wall-parallel direction. The height of the first layer next to the cylinder is $5.0 \times 10^{-4}D$. These grid parameters are based on the direct numerical simulation of Jiang et al.[37]. The outflow boundary was imposed by Gresho's method[38].

A fine grid with twice the number of cells in the wall-normal and wall-parallel directions, respectively, was prepared. Numerical simulations were performed for $Re = 300$ on the fine and regular grids. The time step size is set such that the maximum CFL number across all cells is less than or equal to 1.0. The definition of CFL is the same as in the previous study[39]. On the regular grid, simulation was also performed with a CFL of less than 0.5 with half the time interval. Figure 2 shows the spatial distributions of the time-averaged velocity field at $x/D = 1$, 3, and 5 for each simulation case. The mean fields obtained from all three simulations are in close agreement. In this paper, simulations with a CFL number of 1.0 on a regular grid are accurate enough because we only deal with flows around two-dimensional cylinders whose Re is smaller than 300.

4 Results of ROM

4.1 Based-on POD Mode of $Re = 80$

The pressure ROM is constructed for flow around a circular cylinder. A numerical simulation of cylinder flow at $Re = 80$ was performed to obtain the POD dataset. The POD modes were obtained by time-

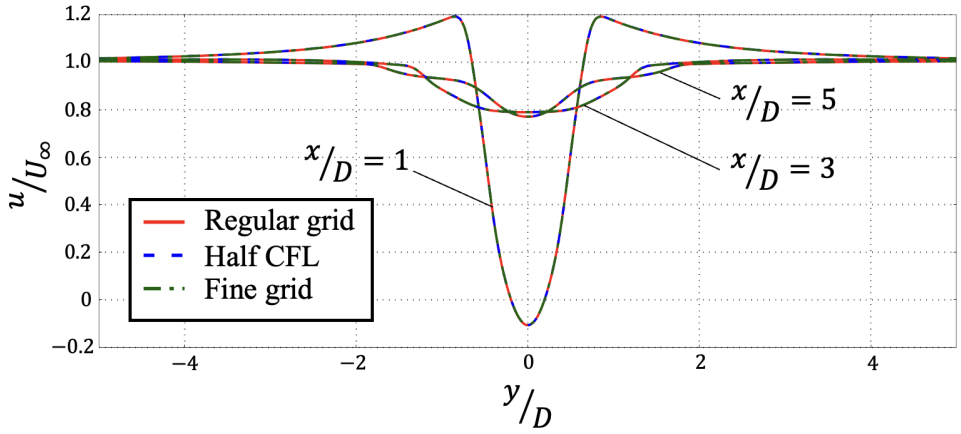

(a) x-direction velocity

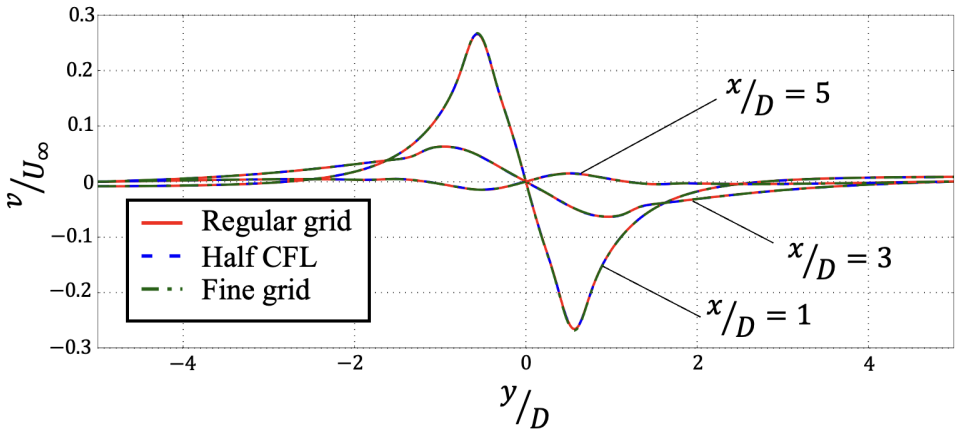

(b) y-direction velocity

Figure 2: Comparison of x- and y-directional velocity distributions in the wake of a cylinder between a regular grid, a fine grid with a CFL of less than 0.9, and a regular grid with half the CFL. At all positions $x/D = 1, 3, 5$, the spatial distributions are completely consistent. Hence, all numerical simulations in this study are performed on a regular grid with a CFL of less than 1.0.

series pressure fields. Figure 3 shows the top four POD modes with the largest eigenvalues and the pressure mean field. POD mode has a paired spatial structure with 1st and 2nd mode, 3rd and 4th mode, respectively. The spatial scale of the wake vortex is smaller as the rank of the mode decreases. The POD successfully captures the periodic vortex structure in the wake in a two-dimensional unsteady flow around a cylinder.

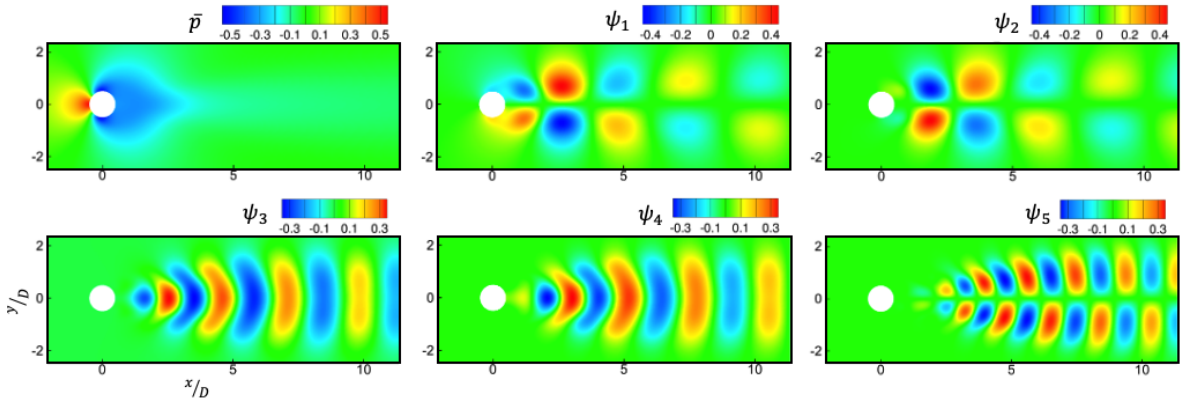

Figure 3: Pressure mean-field and 1st to 4th POD modes obtained from the pressure field around a cylinder with $Re = 80$.

An ROM for the pressure field was constructed using the POD modes of flow around a cylinder with a $Re = 80$. The velocity field at the same Re of POD mode was given for the ROM to predict the pressure field. The pressure fields obtained by ROM and by full-order numerical simulations are shown in Fig. 4. The results reconstructed by the ROM are in complete agreement with the numerical simulation results.

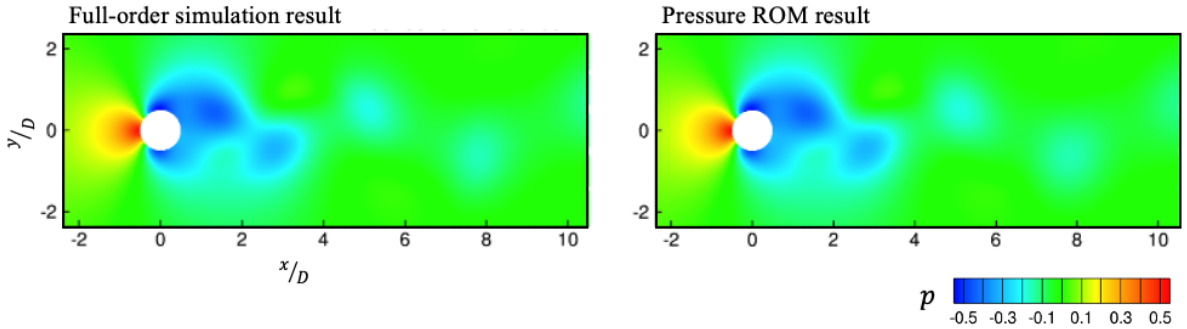

Figure 4: Comparison of instantaneous pressure coefficients on cylinder surface at $Re = 80$ obtained from full-order numerical simulation and ROM. ROM is constructed using pressure POD mode obtained from $Re = 80$. Two pressure coefficients are in complete agreement.

The pressure coefficient C_p was computed from the pressure field as

$$C_p = \frac{\hat{p} - \hat{p}_\infty}{\frac{1}{2}\rho U_\infty^2}, \tag{17}$$

where $\hat{p}$ is the dimensional pressure and $\hat{p}_\infty$ is the dimensional far-field pressure. The pressure coefficient distribution on the cylinder surface is shown in Fig. 5. The Cp distributions are completely matched. Therefore, the ROM can accurately compute the pressure field under the same conditions as the POD modes. In the velocity field ROM using Galerkin projection, it is well known that even under the same conditions as in the POD modes, the ROM results are not exactly the same as the full-order numerical simulation [40, 15]. ROM for pressure fields tends to yield closer results to full-order numerical simulation than ones for velocity fields.

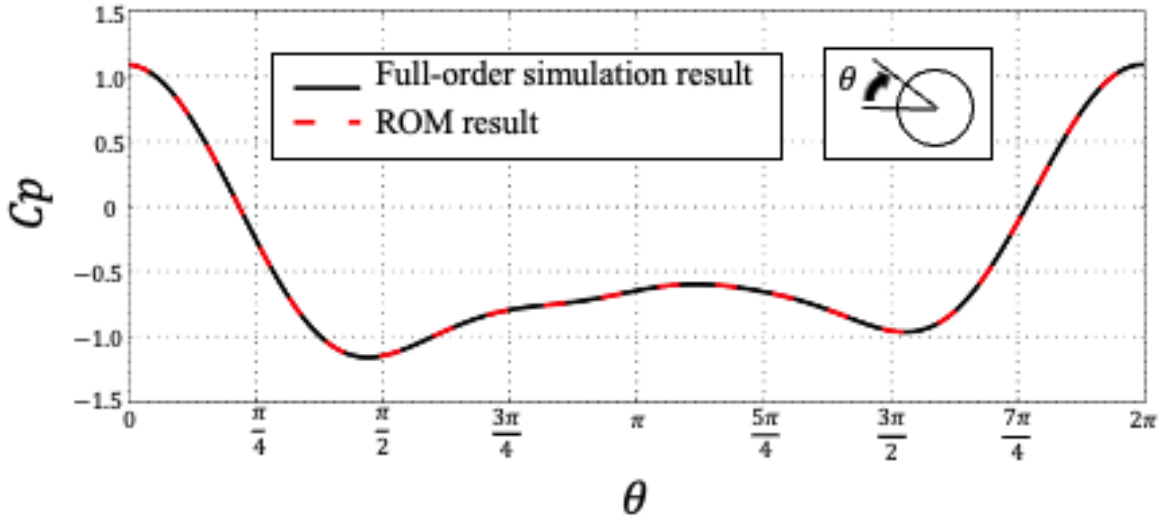

Figure 5: Comparison of instantaneous pressure field at $Re = 80$ obtained from full-order numerical simulation and ROM. ROM is constructed using pressure POD mode obtained from $Re = 80$.

The pressure field was computed by giving the velocity field at $Re = 120$, which was different from the pressure field condition $Re = 80$, where the POD mode was obtained. Figure 6 shows the pressure field obtained from the ROM and the pressure field in the full-order numerical simulation simultaneously with the given velocity field. Compared with the reconstruction results of the pressure field under the conditions $Re = 80$, the difference from the full-order numerical simulation is remarkable. Particularly, the distribution of the wake, indicated by the red circle in the figure, is completely different. ROM also underestimates pressure fluctuations in the cylinder wake $\frac{x}{D} > 2$. ROM cannot always accurately predict the pressure field, which differs from the conditions under which the POD mode was obtained.

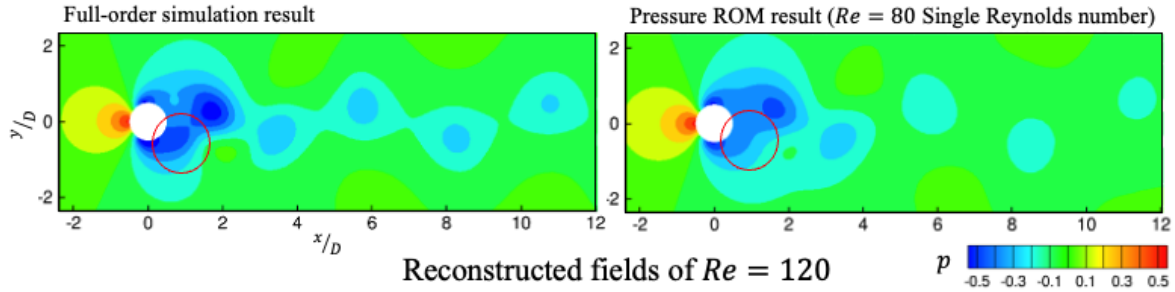

Figure 6: Comparison of instantaneous pressure fields between two ROMs and numerical results. In the red circle region, the ROM cannot predict the numerical results.

The pressure field was reconstructed at $Re = 50$–180. In this range, we reconstructed 501 time series data with $\Delta t = 0.1$ for each Re. Mean squared errors were computed on the 501 reconstructed snapshots, and the pressure field was simultaneously obtained from the full-order numerical simulations. The mean squared error was defined as:

$$M.S.E. = \frac{1}{T}\int_T \frac{\int_V (p(\boldsymbol{x},t) - p'(\boldsymbol{x},t))^2 d\boldsymbol{x}}{\int_V p(\boldsymbol{x},t)^2 d\boldsymbol{x}} dt, \tag{18}$$

where T represents the integration time in averaging and $p'(\boldsymbol{x},t)$ is the reconstructed pressure field. This is the reconstruction error defined by the inner product used in the POD methodology, normalized by the squared quantity and time average. The mean squared error at each Re is shown in Fig. 7. The mean squared error is extremely small at $Re = 80$, which is the same condition under which the POD modes were obtained. In contrast, the mean squared errors for all but $Re = 80$ are greater than $\mathcal{O}(10^{-3})$. This difference is reflected in the difference in pressure distribution in Fig. 6. Therefore, the POD modes obtained from $Re = 80$ are not valid for predicting the pressure field of different Re.

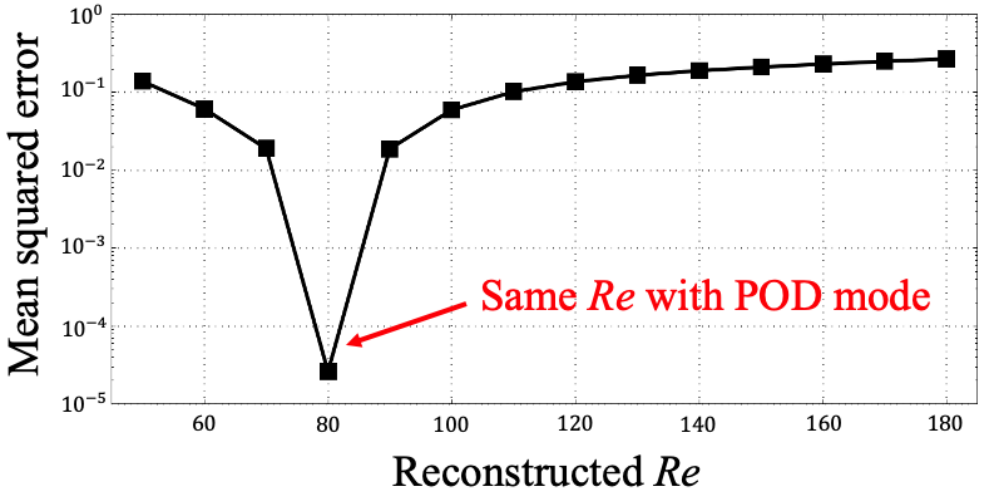

Figure 7: Mean squared error of pressure fields between full-order numerical simulation and ROM. ROM is constructed by the POD modes at $Re = 80$. The mean squared error is minimized at $Re = 80$ under the same conditions as POD modes. The mean squared error is extremely large under conditions different from the POD modes. ROM of pressure field constructed using the POD modes under a single condition lacks robustness.

4.2 Based-on Global POD Mode of $Re = 80$ and 160

In this section, a snapshot of the pressure field at $Re = 160$ is included in the dataset in addition to $Re = 80$. The POD was performed on the dataset containing two Re's, and a set of the global POD modes representing the pressure field of the two Re's was obtained. The global POD mode and average pressure field obtained from $Re = 80$ and 160 are shown in Fig. 8. The spatial distributions of the average pressure field, 1st POD mode, and 3rd POD mode are similar to those of the POD mode obtained from $Re = 80$. Unlike the 1st and 3rd modes, the 2nd mode has a vertically symmetrical structure like an average pressure field. In the global POD, the time-averaged flow component exists in the dataset with the same number of conditions. That is, there are two features in the dataset that have a vertically symmetric spatial distribution at $Re = 80$ and 160. Therefore, in addition to the mean field, a POD mode with a vertically symmetric distribution is needed to represent the dataset. Similar results have been obtained in previous studies on the global POD modes derived from velocity fields[20, 19]. The 4th and 5th modes have a distribution similar to the 1st and 3rd modes. These are POD modes that represent the pressure field at $Re = 160$, as it is different from the mode at $Re = 80$. Thus, the global POD modes capture the spatial distribution of the pressure field for both $Re = 80$ and $Re = 160$.

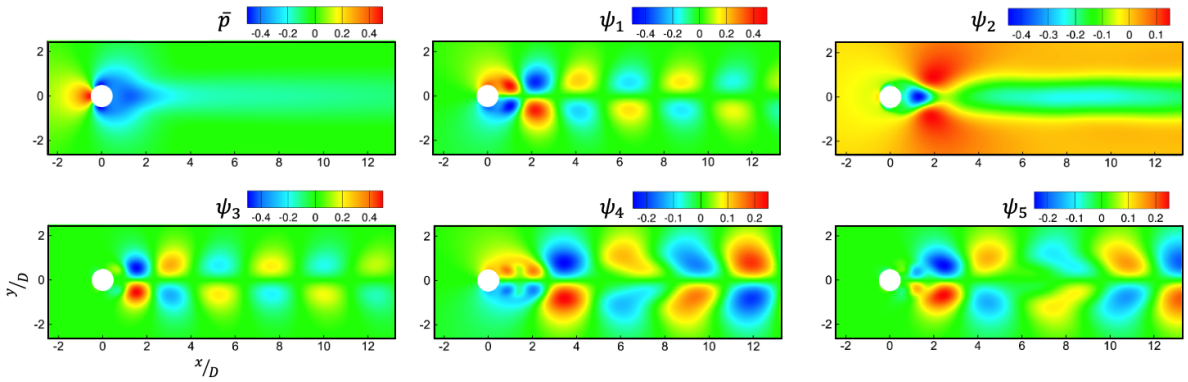

Figure 8: Spatial distribution of the mean field and 1st to 5th global POD modes obtained from pressure fields at $Re = 80$ and 160.

The ROM for the pressure field was constructed using the global POD modes. The results of the pressure field computed by ROM for $Re = 120$, and the instantaneous pressure field obtained from

the full-order numerical simulation are shown in Fig. 9. Although the pressure field is under different conditions from those in the POD modes, the pressure field obtained from the ROM closely reproduces the results of the full-order numerical simulation. Compared to the results predicted by the ROM constructed with the POD modes of $Re = 80$ in Fig. 6, the global POD modes capture the characteristics of the pressure field behind the cylinder. The ROM based on the global POD also accurately evaluates the pressure fluctuations at $\frac{x}{D} > 2$.

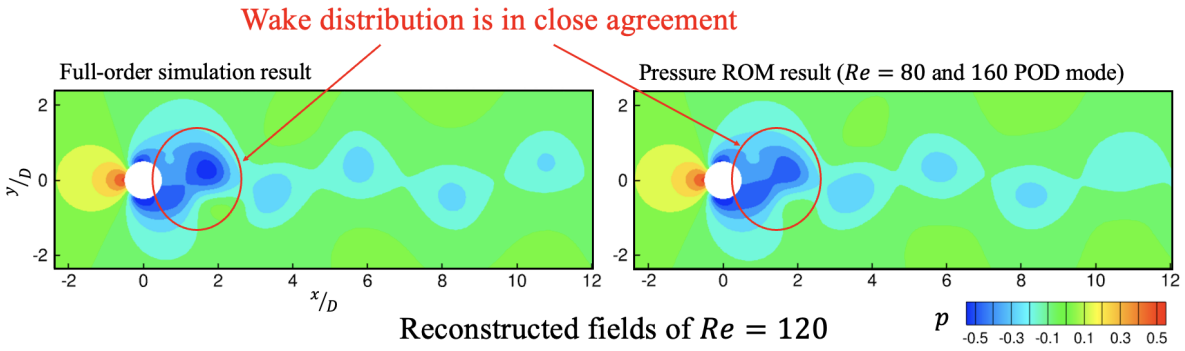

Figure 9: Comparison of instantaneous pressure fields at $Re = 120$ between single POD-based ROM, global POD-based ROMs, and numerical results. In the red circle region, the global ROM predicts the numerical results more accurately than the single ROM.

The mean squared error was computed for $Re = 50$–180, as in the computation of ones in Fig. 7. Figure 10 shows the mean squared error in the ROMs using the global POD modes and the POD modes of $Re = 80$. In terms of the prediction of the pressure field at $Re = 80$, the ROM using the global POD modes is inferior to the ROM using the POD modes of $Re = 80$. However, for pressure fields other than $Re = 80$, the ROM using the global POD modes has a smaller mean squared error than the ROM using the POD modes of $Re = 80$. The mean squared error is significantly small at $Re = 160$ in the ROM using the global POD modes. This is because the dataset contains the pressure field at $Re = 160$ when the global POD modes are obtained. The ROM using the global POD modes has a small mean squared error even for the pressure field of different Re from that contained in the dataset. As a result, ROMs using global POD modes are highly robust against Re.

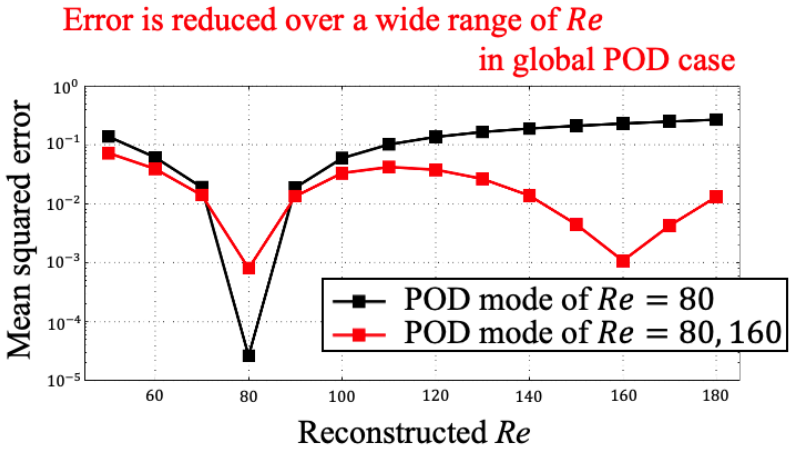

Figure 10: Comparison of mean squared error between two ROMs and full-order numerical results. ROMs constructed using the POD modes from pressure fields at multiple Re's have small mean squared errors even at Re, which are different from those in the dataset. Compared to the ROM constructed using the POD modes from a single Re pressure field, the ROM constructed using the POD modes obtained from multiple Re's is more robust.

4.3 Mode Number Effect

We investigate the robustness improvement when the number of modes used for ROM is changed. ROMs were constructed by changing the number of POD modes obtained from $Re = 80$ and global POD modes obtained from $Re = 80$ and 160, respectively. Figure 11 shows the mean squared error for the ROM using the POD modes of $Re = 80$ with the different number of modes r. As the number of modes increases from 6 to 10, only the mean squared error for $Re = 80$ decreases. Since there is no effect on the other Re, the increase in the number of modes does not significantly improve the robustness of the ROM using the POD modes with $Re = 80$.

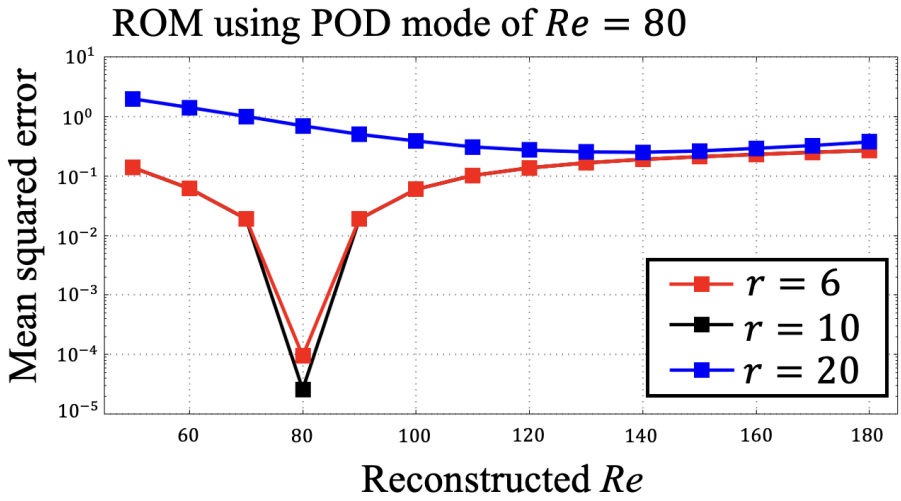

Figure 11: Comparison of mean squared error between three different numbers of mode r. ROM is constructed using POD modes obtained from the pressure field with $Re = 80$. Increasing the number of modes does not contribute to the reduction of the mean squared error under conditions different from those of the POD modes. Excessive increase in the number of modes results in an increase in the mean squared error.

Remarkably, the mean squared error increases overall as the number of modes increases from 10 to 20. In order to identify the mode responsible for this increase, we computed the mean squared error when the number of modes was 12, 14, 16, and 18. Figure 12 shows the mean squared error when the number of modes is 14 and 16. The large gap is found in the mean squared error when the number of modes changes from 14 to 16.

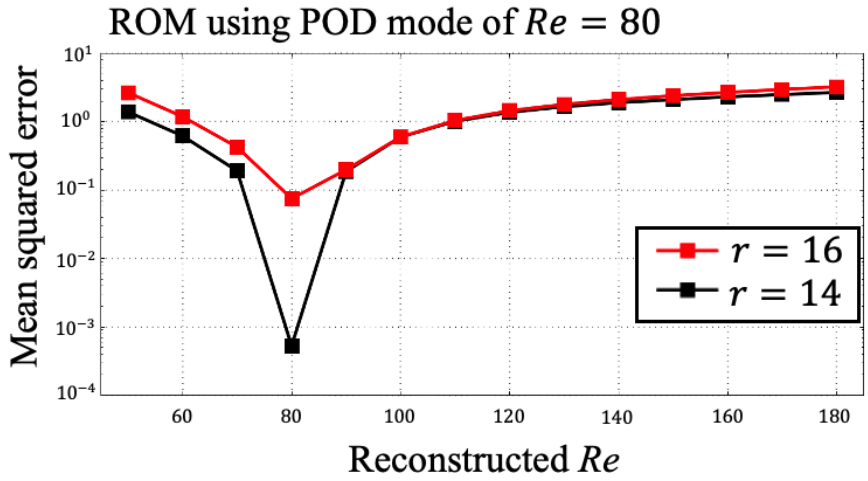

Figure 12: Comparison of the mean squared error when the number of modes r is 14 and 16. An increase in the mean squared error is occurring between 14 and 16. This suggests that the 15th or 16th mode is increasing the mean squared error

The 15th mode that may have produced this difference is shown in Fig. 13. Numerical errors are

found near the far-field boundary of this mode. No such numerical error is found in the POD modes until the 14th. The location of these errors is where the inflow and outflow boundary conditions are interchanged. The 15th POD mode captures this small numerical error in the pressure field. The coefficient corresponding to this POD mode was not computed accurately in the ROM, which is the reason for the increase in the mean squared error. Therefore, an excessive increase in the number of POD modes may lead to an increase in errors due to numerical errors. Regardless of the case, the POD mode obtained from a single Re does not improve robustness even if the number of modes is increased.

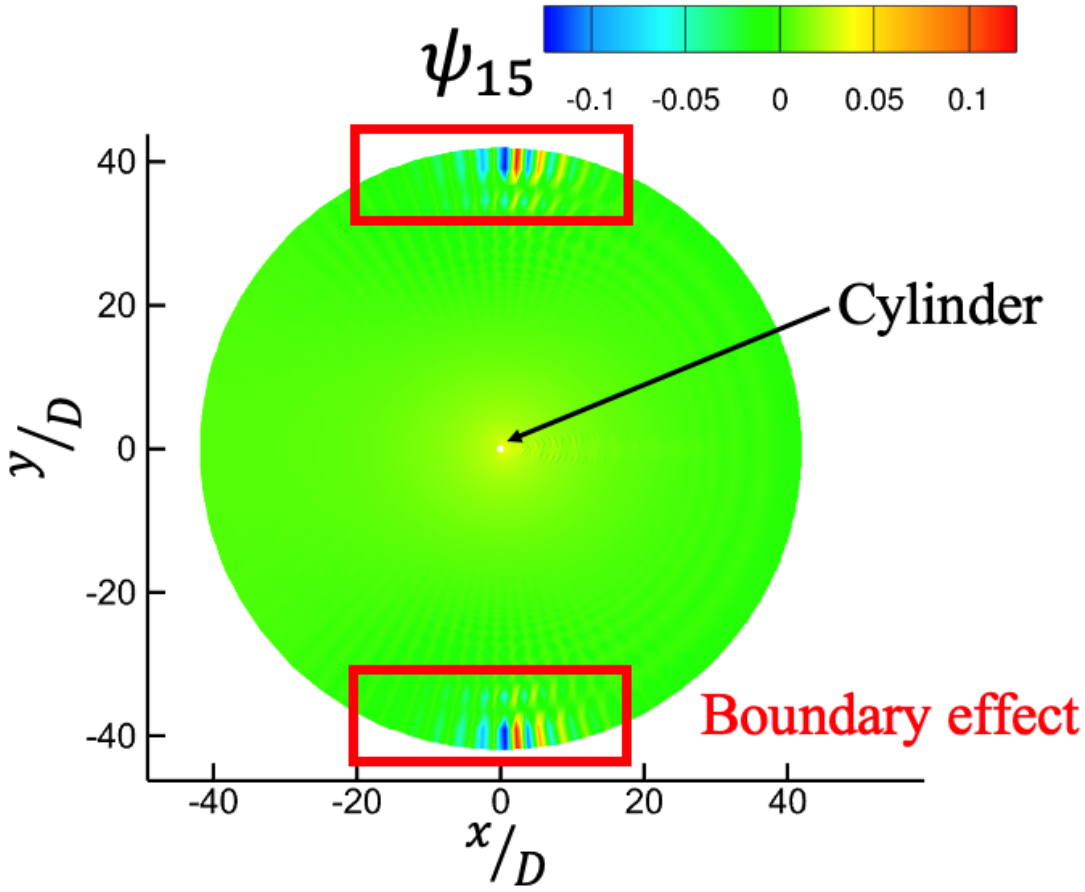

Figure 13: Spatial distribution of the 15th POD mode obtained from the pressure field at $Re = 180$. Non-physical errors are observed near the far boundary. Such errors do not exist in the spatial distribution of POD mode up to the 14th. This error leads to an increase in mean squared error.

Figure 14 shows the mean squared error for the ROM using the POD modes of $Re = 80$ and 160 with the different number of modes r. The overall mean squared error drops as the number of modes increases from 6 to 10. When $r = 10$ is increased to 20, the mean squared error does not decrease except for $Re = 80, 150, 160$, and 170. There is a slight decrease for $Re = 150$ and 170, but no significant difference compared to when the number of modes is increased from 6 to 10. Because the higher modes have a smaller contribution to the pressure field, the 10th and higher modes produce a reduction in error of about $\mathcal{O}(10^{-3})$. Therefore, increasing the number of modes improves the robustness of the global POD-based ROM, but an excessive increase is unnecessary.

The mean squared error in the ROM based on the global POD does not show a significant increase, as occurred in the single POD when the number of modes was increased to $r = 20$. This is because the global POD modes up to the 20th do not contain numerical errors derived from the boundary conditions. However, when focusing on the lower-ranked modes, such errors were found in the 34th global POD mode. Therefore, increasing the excessive number of POD modes, even in the global POD, introduces the numerical errors derived from boundary conditions.

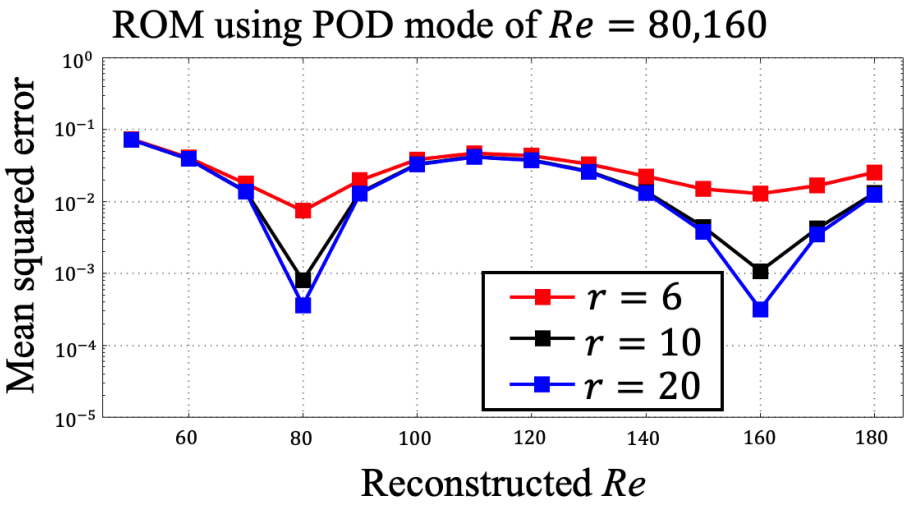

Figure 14: Comparison of mean squared error between three different numbers of mode r. ROM is constructed using POD modes obtained from the pressure field with $Re = 80, 160$. Increasing the mode from $r = 6$ to 10 decreases the mean squared error for different Re from the dataset. Increasing $r = 10$ to 20 decreases the mean squared error only at the same Re as the dataset. Excessively increasing the number of POD modes does not improve robustness.

The dataset was composed of time-series data of the pressure fields at Re = 80,120, and 160. The global POD modes were obtained from this dataset. ROMs were constructed for different numbers of the POD modes to predict the pressure field. The mean squared error between the pressure fields obtained from the ROM and the full-order numerical results is shown in Fig. 15. The mean squared error in the pressure field of Re outside the dataset is almost the same as that of Re contained in the dataset. The mean squared error decreased for all Re when the number of modes was increased from 10 to 20. The ROM results (Fig. 14) obtained from datasets with Re = 80 and 160 show that when the number of modes is larger than 10, the mean squared error of Re, which is different from that of the dataset, does not decrease. Therefore, as the number of Re's in the dataset increases, more modes can be used to effectively improve robustness. The decrease in the mean squared error is small for pressure fields where Re is smaller than 80. For the dataset, Re, less than 80 is an extrapolation region, so the mean squared error may not decrease as much. Consequently, it is effective to include more conditions in the dataset to improve the robustness of the pressure field ROM.

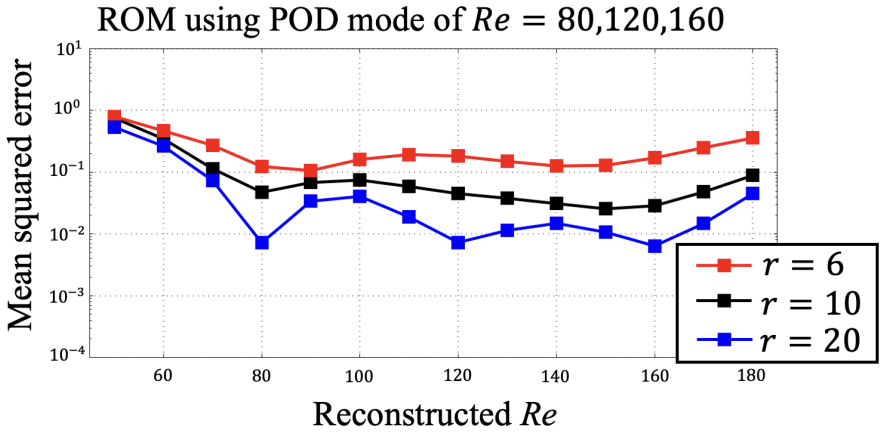

Figure 15: Comparison of mean squared error between three different numbers of mode r. ROM is constructed using POD modes obtained from the pressure field with Re = 80, 120, and 160. Mean squared error decreases for most Re by increasing r. Increasing the number of conditions included in the dataset is expected to improve robustness.

5 Conclusion

In this study, we proposed a POD-based ROM for the pressure field. ROM with the POD mode derived from time series data at a single Re accurately predicts the pressure field at the same Re. However, when the pressure field with a Re different from that of the POD modes is predicted, the accuracy of the prediction is significantly reduced. Increasing the number of POD modes does not improve the prediction accuracy in this case. We also found that an excessive number of modes increases the mean squared error of all Re due to numerical errors contained in the higher modes.

The ROM was constructed using the global POD that included multiple Re's pressure fields in the dataset. The ROM using the global POD mode improved prediction accuracy over a wide range for Re different from the data. In addition, a sufficient number of modes achieved high robustness. Thus, the global POD-based pressure ROM is more robust to Re variation than the ROM based on the POD for a single condition. In the global POD-based ROM, numerical error is observed in the higher modes. The mode comtains numercal error would reduce the prediction accuracy of global POD-based ROM. Based on these results, a global POD-based ROM for pressure fields achieves high robustness by selecting the appropriate number of modes.

ACKNOWLEDGEMENTS

The numerical simulation is performed on the Supercomputer system "AFI-NITY" at the Advanced Fluid Information Research Center, Institute of Fluid Science, Tohoku University, and JAXA Supercomputer System Generation 3 (JSS3). This work was partially supported by the Sasakawa Scientific Research Grant from The Japan Science Society. This work was also partially supported by JST SPRING, Grant Number JPMJSP2114, Japan.

A Incremental POD

A.1 Incremental POD methodology

The POD modes can be computed from a sufficiently large number of grids, or a sufficiently large number of data, with limited memory. In such situations, a method referred to as incremental POD is used. In incremental POD, POD is performed on a portion of the data $u_m(m = 1, 2, \cdots, m_0)$ selected from all the data $u_m(m = 1, 2, \cdots, m_{\max}; m_{\max} > m_0)$. The covariance matrix S_{m_0} constructed from some of this data is approximated as $S_{m_0} \approx U_{m_0} D_{m_0} U_{m_0}^T$, where D_{m_0} is $m_r \times m_r$ $(m_r < m_0)$ matrix, and U_{m_0} is $m_r \times n$ matrix.

A data u_{m_0+1} is selected from the dataset, and POD mode is updated to represent this data. The mean component of m_0 data $\bar{u}_{m_0}$ is subtracted from the u_{m_0+1} to compute the fluctuating component $\tilde{u}_{m_0+1} = u_{m_0+1} - \bar{u}_{m_0}$. A projection of the fluctuating component onto U_{m_0} is performed as $\hat{u}_{m_0+1} = U_{m_0} \tilde{u}_{m_0+1}$, and the error for pre and post-projection is computed $\tilde{u}^{\perp}_{m_0+1} = \tilde{u}_{m_0+1} - U^T_{m_0} U_{m_0} \tilde{u}_{m_0+1}$. Then, we can update an approximate covariance matrix

$$S_{m_0+1} = \left[U_{m_0} \quad \frac{\hat{u}_{m_0+1}}{\|\hat{u}_{m_0+1}\|^2} \right] Q^{Inc}_{m_0+1} \left[U_{m_0} \quad \frac{\hat{u}_{m_0+1}}{\|\hat{u}_{m_0+1}\|^2} \right]^T, \tag{19}$$

where

$$Q^{Inc}_{m_0+1} = \begin{bmatrix} D_{m_0} + \hat{u}_{m_0+1} \hat{u}^T_{m_0+1} & \|\tilde{u}^{\perp}_{m_0+1}\| \hat{u}_{m_0+1} \\ \|\tilde{u}^{\perp}_{m_0+1}\| \hat{u}^T_{m_0+1} & \|\tilde{u}^{\perp}_{m_0+1}\|^2 \end{bmatrix}. \tag{20}$$

$Q^{Inc}_{m_0+1}$ is diagonalized by a matrix $D^{Inc}_{m_0+1}$ consisting of eigenvectors $U^{Inc}_{m_0+1}$ and eigenvalues. The eigenvalues D_{m_0+1} and eigenvectors U_{m_0+1} can be calculated by

$$U_{m_0+1} = \left[U_{m_0} \quad \frac{\hat{u}_{m_0+1}}{\|\hat{u}_{m_0+1}\|^2} \right] U^{Inc}_{m_0+1}, \tag{21}$$

$$D_{m_0+1} = D^{Inc}_{m_0+1}. \tag{22}$$

A.2 Validation of Incremental POD

The eigenvalues and eigenvectors are compared for a flow around a cylinder with a $Re = 100$ by performing a non-incremental POD and the incremental POD. The time series flow data comprises 501 snapshots sampled at 0.1 intervals for 50 dimensionless times. The incremental POD was performed with $m_0 = 301$, and the POD mode was updated incrementally in the other 200 data. The eigenvalues and contribution ratios obtained from the two PODs are shown in Table 1. The eigenvalues magnitudes for 1st to 6th POD modes are almost identical for the two PODs. The largest difference in the contribution ratio of each mode obtained for the two PODs is 0.01%. Therefore, when the number of modes is determined such that cumulative contribution ratios exceed 99.9%, the number of modes selected for incremental and non-incremental PODs is the same.

Table 1: Comparison of eigenvalues and contribution ratios obtained from non-incremental and incremental POD. Minimum number of modes with a cumulative contribution exceeding 99.9% is six for both of the two PODs. The differences in eigenvalues and contribution rates obtained for the two PODs do not affect the choice of the number of modes when the number of modes is determined based on 99.9%.

	Eigenvalue		Contribution ratio [%]	
	Non-incremental	Incremental	Non-incremental	Incremental
1st mode	1836.1520	1838.0653	49.486040	49.487315
2nd mode	1764.197	1765.9426	47.546783	47.545512
3rd mode	38.002	38.041202	1.024191	1.024205
4th mode	37.5804	37.61803	1.012826	1.012813
5th mode	16.0825	16.098745	0.433439	0.433436
6th mode	15.9768	15.993012	0.43059	0.430588
cumulative ratio	-	-	99.933869	99.933869

We focus on the spatial distribution of POD modes up to 6th mode in the two PODs. The spatial distribution of the POD mode along the axis of the cylinder wake is shown in Fig. 16. From the one-dimensional plot for PDO modes, non-incremental and incremental POD modes are consistent for 1st to 6th modes. Therefore, the incremental POD is beneficial as a method to obtain POD mode.

References

[1] D. J. Lucia, P. S. Beran, and W. A Silva. Reduced-order modeling: new approaches for computational physics. *Progress in aerospace sciences*, 40(1-2):51–117, 2004.

[2] H. Kang, Z. Tian, G. Chen, L. Li, and T. Wang. Application of POD reduced-order algorithm on data-driven modeling of rod bundle. *Nuclear Engineering and Technology*, 54(1):36–48, 2022.

[3] K. Lu, Y. Jin, Y. Chen, Y. Yang, L. Hou, Z. Zhang, Z. Li, and C. Fu. Review for order reduction based on proper orthogonal decomposition and outlooks of applications in mechanical systems. *Mechanical Systems and Signal Processing*, 123:264–297, 2019.

[4] R. Vinuesa and S. L. Brunton. Enhancing computational fluid dynamics with machine learning. *Nature Computational Science*, 2(6):358–366, 2022.

[5] C. W. Rowley and S. T. M. Dawson. Model reduction for flow analysis and control. *Annual Review of Fluid Mechanics*, 49(1):387–417, 2017.

[6] S. L. Brunton, B. R. Noack, and P. Koumoutsakos. Machine learning for fluid mechanics. *Annual Review of Fluid Mechanics*, 52(1):477–508, 2020.

[7] J. L. Lumley. The structure of inhomogeneous turbulent flows. *Atmospheric turbulence and radio wave propagation*, 166–178, 1967.

[8] G. Berkooz, P. Holmes, and J. L Lumley. The proper orthogonal decomposition in the analysis of turbulent flows. *Annual review of fluid mechanics*, 25(1):539–575, 1993.

[9] A. Chatterjee. An introduction to the proper orthogonal decomposition. *Current science*, 808–817, 2000.

[10] Y. C. Liang, H. P. Lee, S. P. Lim, W. Z. Lin, K. H. Lee, and C. G. Wu. Proper orthogonal decomposition and its applications—Part I: Theory. *Journal of Sound and vibration*, 252(3):527–544, 2002.

[11] K. Taira, S. L. Brunton, S. T. Dawson, C. W. Rowley, T. Colonius, B. J. McKeon, O. T. Schmidt,

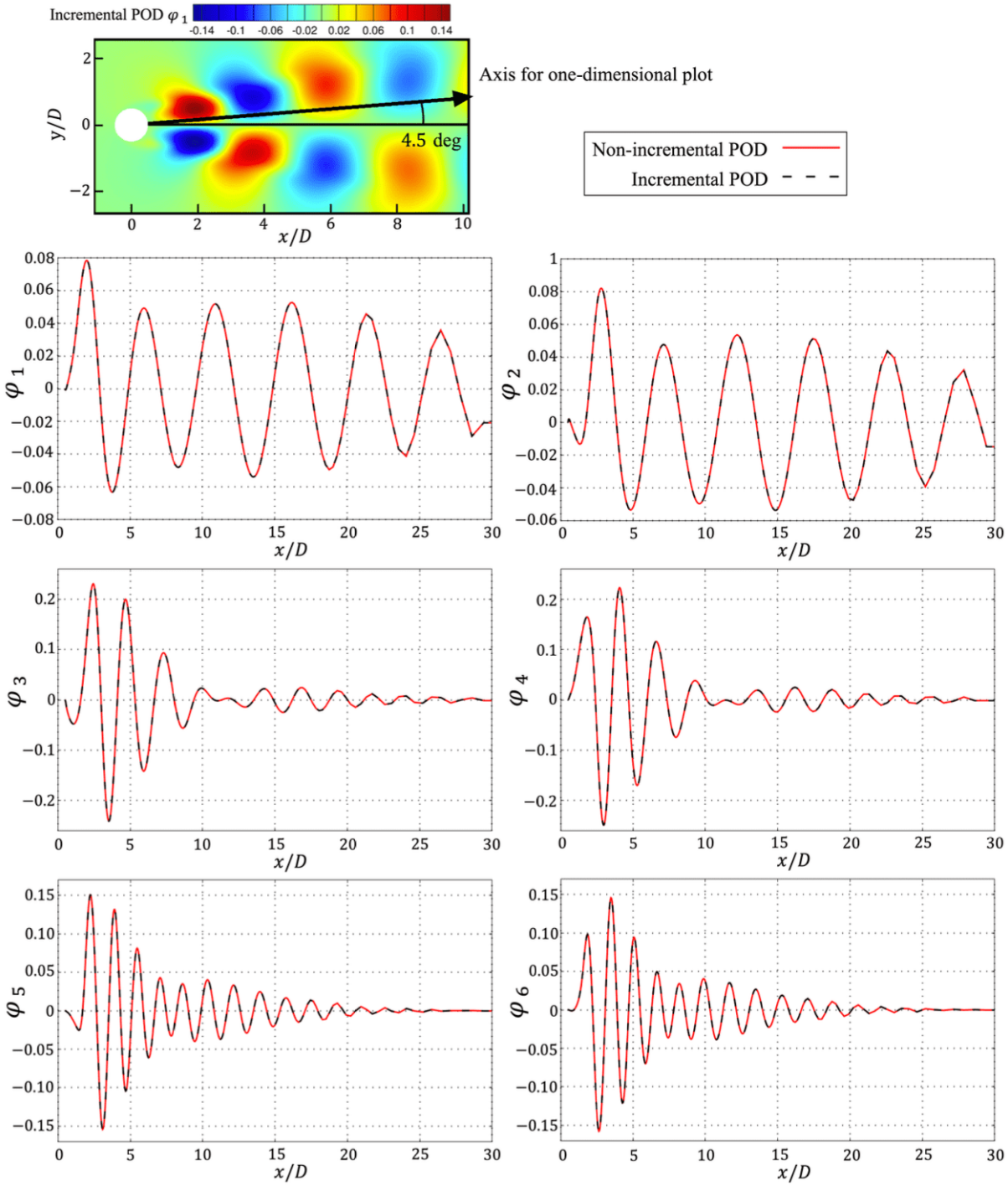

Figure 16: 1st to 6th POD modes obtained from non-incremental and incremental POD. 1D plots show the distribution of POD modes on the axes shown in the top figure. Spatial distribution is consistent for all modes for non-incremental and incremental POD.

S. Gordeyev, V. Theofilis, and L. S. Ukeiley. Modal analysis of fluid flows: An overview. *AIAA Journal*, 55(12):4013–4041, 2017.

[12] K. Taira, M. S. Hemati, S. L. Brunton, Y. Sun, K. Duraisamy, S. Bagheri, S. T. Dawson, and C.-A. Yeh. Modal analysis of fluid flows: Applications and outlook. *AIAA Journal*, 58(3):998–1022, 2020.

[13] S. Sato, H. Sakamoto, and N. Ohnishi. Connections between the modes of a nonlinear dynamical system on a manifold. *Physical Review E*, 103(6), 2021.

[14] O. San, R. Maulik, and M. Ahmed. An artificial neural network framework for reduced order modeling of transient flows. *Communications in Nonlinear Science and Numerical Simulation*,

77:271–287, 2019.

[15] B. R. Noack, K. Afanasiev, M. Morzyński, G. Tadmor, and F. Thiele. A hierarchy of low-dimensional models for the transient and post-transient cylinder wake. *Journal of Fluid Mechanics*, 497:335–363, December 2003.

[16] W. Stankiewicz, M. Morzyński, B. R. Noack, and G. Tadmor. Reduced order Galerkin models of flow around NACA - 0012 airfoil. *Mathematical Modelling and Analysis*, 13(1):113–122, 2008.

[17] L. Cordier, B. Abou El Majd, and J. Favier. Calibration of POD reduced - order models using Tikhonov regularization. *International Journal for Numerical Methods in Fluids*, 63(2):269–296, 2009.

[18] M. Hess, A. Alla, A. Quaini, G. Rozza, and M. Gunzburger. A localized reduced-order modeling approach for PDEs with bifurcating solutions. *Computer Methods in Applied Mechanics and Engineering*, 351:379–403, 2019.

[19] Y. Nakamura, S. Sato, and N. Ohnishi. Improvement of reduced-order model based on global pod in terms of robustness and computational speed. *In preparation.*

[20] Y. Nakamura, S. Sato, and N. Ohnishi. Proper orthogonal decomposition method of constructing a reduced-order model for solving partial differential equations with parametrized initial values. *Partial Differential Equations in Applied Mathematics*, 9:100654, 2024.

[21] R. Schmit and M. Glauser. Improvements in low dimensional tools for flow-structure interaction problems: Using Global POD. In *42nd AIAA Aerospace Sciences Meeting and Exhibit*. American Institute of Aeronautics and Astronautics, 2004.

[22] R. Zimmermann and S. Görtz. Non-linear reduced order models for steady aerodynamics. *Procedia Computer Science*, 1(1):165–174, 2010.

[23] Z. Chen, Y. Zhao, and R. Huang. Parametric reduced-order modeling of unsteady aerodynamics for hypersonic vehicles. *Aerospace Science and Technology*, 87:1–14, 2019.

[24] Y. Nakamura, S. Sato, and N. Ohnishi. Application of proper orthogonal decomposition to flow fields around various geometries and reduced-order modeling. *In preparation.*

[25] B. W. van Oudheusden. PIV-based pressure measurement. *Measurement Science and Technology*, 24(3):032001, 2013.

[26] I. Akhtar, A. H. Nayfeh, and C. J. Ribbens. On the stability and extension of reduced-order Galerkin models in incompressible flows: a numerical study of vortex shedding. *Theoretical and Computational Fluid Dynamics*, 23:213–237, 2009.

[27] I. Akhtar. *Parallel Simulation, Reduced-Order Modeling, and Feedback Control of Vortex Shedding using Fluidic Actuators*. PhD thesis, Virginia Polytechnic Institute and State University, 2008.

[28] L. Sirovich. Turbulence and the dynamics of coherent structures: Parts i–iii. *Quarterly of Applied Mathematics*, 45(3):561–590, 1987.

[29] R. Arora, A. Cotter, K. Livescu, and N. Srebro. Stochastic optimization for PCA and PLS. In *2012 50th annual allerton conference on communication, control, and computing (allerton), 861–868*. IEEE, 2012.

[30] Y. Ohmichi, T. Ishida, and A. Hashimoto. Numerical investigation of transonic buffet on a three-dimensional wing using incremental mode decomposition. *AIAA Paper, 2017-1436*, 2017.

[31] H. Le and P. Moin. An improvement of fractional step methods for the incompressible Navier-Stokes equations. *Journal of Computational Physics*, 92(2):369–379, 1991.

[32] T. Kajishima and K. Taira. *Computational Fluid Dynamics Incompressible Turbulent Flows*. Springer, 2017.

[33] B. P. Leonard. A stable and accurate convective modelling procedure based on quadratic upstream interpolation. *Computer Methods in Applied Mechanics and Engineering*, 19(1):59–98, 1979.

[34] H. A. van der Vorst. Bi-CGSTAB: A fast and smoothly converging variant of Bi-CG for the solution of nonsymmetric linear systems. *SIAM Journal on Scientific and Statistical Computing*, 13(2):631–644, 1992.

[35] M.D. Pocock and S.P. Walker. The complex bi-conjugate gradient solver applied to large electromagnetic scattering problems, computational costs, and cost scalings. *IEEE Transactions on Antennas and Propagation*, 45(1):140–146, 1997.

[36] K. Nakajima, H. Nakamura, and T. Tanahashi. *Parallel iterative solvers with localized ILU preconditioning, 342–350*. Springer Berlin Heidelberg, 1997.

[37] H. Jiang, L. Cheng, S. Draper, H. An, and F. Tong. Three-dimensional direct numerical simulation of wake transitions of a circular cylinder. *Journal of Fluid Mechanics*, 801:353–391, 2016.

[38] P. M. Gresho. Some current CFD issues relevant to the incompressible Navier-Stokes equations. *Computer Methods in Applied Mechanics and Engineering*, 87(2–3):201–252, 1991.

[39] Y. Zang, R. L. Street, and J. R. Koseff. A non-staggered grid, fractional step method for time-dependent incompressible Navier-Stokes equations in curvilinear coordinates. *Journal of Computational Physics*, 114(1):18–33, 1994.

[40] A. E. Deane, I. G. Kevrekidis, G. E. Karniadakis, and S. A. Orszag. Low-dimensional models for complex geometry flows: Application to grooved channels and circular cylinders. *Physics of Fluids A: Fluid Dynamics*, 3(10):2337–2354, 1991.